



Hydrothermal growth of $\text{Co}_3(\text{OH})_2(\text{HPO}_4)_2$ nano-needles on LaTiO_2N for enhanced water oxidation under visible-light irradiation



Yazhou Zhang, Jinwen Shi*, Cheng Cheng, Shichao Zong, Jiafeng Geng, Xiangjiu Guan, Liejin Guo

International Research Center for Renewable Energy (IRCRE), State Key Laboratory of Multiphase Flow in Power Engineering (MFPE), Xi'an Jiaotong University (XJTU), 28 West Xianning Road, Xi'an, 710049, China

ARTICLE INFO

Keywords:

Photocatalytic water oxidation
Cobalt phosphate
Hydrothermal method
Oxynitride
Heterojunction

ABSTRACT

$\text{Co}_3(\text{OH})_2(\text{HPO}_4)_2/\text{LaTiO}_2\text{N}$ composites with a special microstructure were constructed by in-situ hydrothermally growing $\text{Co}_3(\text{OH})_2(\text{HPO}_4)_2$ nano-needles on the surfaces of LaTiO_2N irregular brick-like chunks. An effective heterojunction in the composites was formed based on the matched band structures and the close interfacial combination between $\text{Co}_3(\text{OH})_2(\text{HPO}_4)_2$ and LaTiO_2N , and thus improved the separation and transfer of photo-generated carriers. Consequently, photocatalytic O_2 -evolution activity of the composites was enhanced up to 3.5 times that of LaTiO_2N .

1. Introduction

Photocatalytic water splitting into H_2 and O_2 is one of the most potential approaches to effectively store solar energy in the form of hydrogen energy [1,2]. Compared with the half reaction of water reduction, the half reaction of water oxidation includes four-electron transfer, and thus is considered as a more complicated and difficult process [3,4]. Many efforts have been taken to profoundly investigate and understand this process. Until now, different types of photocatalysts for water oxidation have been developed [5], and (oxy)nitride photocatalysts, such as TaON [6,7], BaTaO_2N [8–10], LaTiO_2N [11–13], GaN:ZnO [14] and metal-free $\text{g-C}_3\text{N}_4$ [15–17], generally show excellent properties in terms of favorable visible-light absorption and suitable redox potentials [7,12,16].

LaTiO_2N , as a promising photocatalyst with stable perovskite structure, could effectively absorb visible light due to suitable band gap (2.1 eV) [18–20], and shows photocatalytic ability for water oxidation in the presence of suitable sacrificial reagents under visible-light irradiation [13,21]. Many strategies such as doping, constructing solid solutions, loading with guest materials and modifying micro/nano-structures, have been designed to improve the photocatalytic activity for water oxidation on LaTiO_2N [12,13,22–26]. It is worth noting that low-cost cobalt-containing materials like cobalt complexes [27,28], cobalt oxides [12,29–31], cobalt-layered double hydroxides [32–35],

cobalt selenides [36–38] and cobalt phosphate [39–41], showed great potentials as O_2 -evolution electrocatalysts or as guest materials to modify host photocatalysts for high efficiency, which was comparable to that obtained from precious-metal-based materials. It was reported that LaTiO_2N modified with cobalt oxide showed exceedingly better photocatalytic activity for water oxidation than pure LaTiO_2N [13]. Therefore, it was speculated that modification by other cobalt-containing materials might be also feasible to improve the photocatalytic O_2 -evolution performance of LaTiO_2N .

Recently, we have reported that one kind of cobalt phosphate ($\text{Co}_3(\text{OH})_2(\text{HPO}_4)_2$) was prepared by a simple hydrothermal method, and was applied as a novel photocatalyst for water oxidation under visible-light irradiation [42]. This photocatalyst showed a lot of advantages such as excellent crystallinity, good visible-light response and favorable photocatalytic ability [42]. Accordingly, the combination of $\text{Co}_3(\text{OH})_2(\text{HPO}_4)_2$ with LaTiO_2N is proposed to be an effective strategy for better photocatalytic O_2 -evolution activity. Herein, we intended to prepare a series of $\text{Co}_3(\text{OH})_2(\text{HPO}_4)_2/\text{LaTiO}_2\text{N}$ composite photocatalysts with different ratios of $\text{Co}_3(\text{OH})_2(\text{HPO}_4)_2$ and LaTiO_2N by a hydrothermal method, and to comprehensively investigate the physicochemical properties, especially the micro/nano-structures and the interface/surface characteristics, and to further elaborate the enhancement mechanism of photocatalytic water oxidation on composite photocatalysts.

* Corresponding author.

E-mail address: jinwen_shi@mail.xjtu.edu.cn (J. Shi).

2. Experimental section

2.1. Preparation of samples

Preparation of LaTiO_2N : At first, $\text{La}_2\text{Ti}_2\text{O}_7$ (LTO) precursors were synthesized by a polymerized complex method as follows [13]. Citric acid ($\text{C}_6\text{H}_8\text{O}_7\text{H}_2\text{O}$, 0.04 mol), tetraisopropyl titanate ($\text{Ti}(\text{OCH}(\text{CH}_3)_2)_4$, 0.01 mol), lanthanum nitrate ($\text{La}(\text{NO}_3)_3\text{H}_2\text{O}$, 0.01 mol) and ethylene glycol ($\text{C}_2\text{H}_6\text{O}_2$, 0.16 mol) were orderly dissolved into methanol (CH_3OH , 50 mL) with stirring. The obtained clear colloidal solution was heated at 70 °C for 4 h and 130 °C for 20 h. The resulting organic matrix was carbonized at 200 °C for 4 h, 300 °C for 1 h, 350 °C for 1 h and 500 °C for 12 h in sequence to remove organic matters. After cooled naturally to room temperature, the obtained powders (LTO) were grounded and collected, and then treated with a thermal nitridation process to prepare LaTiO_2N (LTON) as follows. The as-prepared LTO powders (1.00 g) were put into a quartz boat (length: 100 mm, diameter: 15 mm), and heated in a Hefei Ke Jing GSL-1700X alumina tube furnace at 950 °C for 15 h under a NH_3 flow (300 mL min⁻¹), and then cooled naturally to room temperature in the NH_3 flow.

Preparation of $\text{Co}_3(\text{OH})_2(\text{HPO}_4)_2/\text{LaTiO}_2\text{N}$ composites: $\text{Co}_3(\text{OH})_2(\text{HPO}_4)_2/\text{LaTiO}_2\text{N}$ composites were prepared by a hydrothermal method. LTON (0.200 g) was added into deionized water (60 mL) with stirring, and further sonicated for 10 min. $\text{Co}(\text{NO}_3)_2$ solution (0.10 M, 3.27 mL) and $(\text{NH}_4)_3\text{PO}_4$ solution (0.10 M, 4.91 mL) were then dropped into the above suspension in order. After stirring for 2 h, additional deionized water (10 mL) was added to obtain a suspension, which was then transferred into a Teflon-lined stainless autoclave and heated in an oven at 200 °C for 6 h without stirring. The precipitation obtained by the hydrothermal process was collected and washed by deionized water and ethanol, and dried at 50 °C for 12 h in a vacuum oven. The obtained sample was labeled as CoPi-H/LTON-33, in which 33 represented a mass ratio of $\text{Co}_3(\text{OH})_2(\text{HPO}_4)_2$ to LaTiO_2N to be 33% by calculation according to the amounts of feed reagents. $\text{Co}_3(\text{OH})_2(\text{HPO}_4)_2/\text{LaTiO}_2\text{N}$ composites with different $\text{Co}_3(\text{OH})_2(\text{HPO}_4)_2$ contents were obtained by changing the amounts of LTON added in the hydrothermal system, and the obtained samples were labeled as CoPi-H/LTON- x , in which $x\%$ represented the mass ratios of $\text{Co}_3(\text{OH})_2(\text{HPO}_4)_2$ to LaTiO_2N . As comparison, LaTiO_2N was treated with the same hydrothermal process in deionized water (8.18 mL) instead of $\text{Co}(\text{NO}_3)_2$ and $(\text{NH}_4)_3\text{PO}_4$ mixed solutions to obtain the sample without $\text{Co}_3(\text{OH})_2(\text{HPO}_4)_2$ (LTON-H). Meanwhile, $\text{Co}_3(\text{OH})_2(\text{HPO}_4)_2$ (CoPi-H) was prepared according to our recent report [42]. Besides, the physical mixture of LaTiO_2N and $\text{Co}_3(\text{OH})_2(\text{HPO}_4)_2$ (CoPi-H + LTON-33) was prepared as follow. $\text{Co}_3(\text{OH})_2(\text{HPO}_4)_2$ (0.066 g) and LaTiO_2N (0.200 g), with a mass ratio of 33%, were added into deionized water (20 mL) and then stirred with a speed of 500 rpm min⁻¹ for 2 h. The resulting suspension was then centrifuged (4000 rpm min⁻¹, 5 min) to obtain precipitates that were finally dried at 50 °C for 12 h in a vacuum oven.

Preparation of LaTiO_2N and $\text{Co}_3(\text{OH})_2(\text{HPO}_4)_2/\text{LaTiO}_2\text{N}$ composite photoanodes: LaTiO_2N photoanode was fabricated by an electro-phoretic deposition (EPD) process followed by a necking treatment [43]. Firstly, LaTiO_2N powder (20 mg), iodine (5 mg) and acetone (20 mL) were mixed with sonication for 40 min and then used for EPD. The EPD process was then carried out between two parallel FTO electrodes with a distance of 1 cm. A direct voltage of 20 V between the two FTO electrodes was kept for 2 min. Secondly, the obtained electrode was dried in air, and then dropped with TiCl_4 methanol solution (50 mM, 30 μL). Finally, the dropped electrode was dried in air, and kept at 500 °C for 30 min under a NH_3 flow (500 mL min⁻¹).

$\text{Co}_3(\text{OH})_2(\text{HPO}_4)_2/\text{LaTiO}_2\text{N}$ composite photoanode was prepared based on the as-prepared LTON photoanode. $(\text{NH}_4)_3\text{PO}_4$ (0.1 M, 400 μL) and $\text{Co}(\text{NO}_3)_2$ (0.1 M, 600 μL) aqueous solutions were dropped into deionized water (60 mL) in order with stirring, and additional deionized water (10 mL) was added after 2 h. The obtained suspension was transferred into a Teflon-lined stainless autoclave, and the as-prepared LTON photoanode was then placed in the Teflon-lined stainless

autoclave as well and kept in an oven at 200 °C for 6 h without stirring. The resulting CoPi-H/LTON photoanode was washed by deionized water and dried in air.

2.2. Characterization

X-ray diffraction (XRD) patterns were measured by a PANalytical X'pert MPD Pro diffractometer with a scan rate of 8.53° min⁻¹ in the 20 range from 10 to 80°. UV-vis spectra were recorded by a Hitachi U-4100 UV-vis-near-IR spectrophotometer with reference to white BaSO_4 . Scanning electron microscopy (SEM) images were obtained with a JEOL JSM-7800F field emitting scanning electron microscope. Transmission electron microscopy (TEM) images of LTON and CoPi-H/LTON-33 were collected by FEI Tecnai G² F30 S-Twin and Titan G² 60–300 transmission electron microscopes, respectively, with an accelerating voltage of 300 kV. Brunauer-Emmette-Teller (BET) surface areas were obtained from the N_2 -adsorption/desorption isotherms, which were recorded by a Micromeritics ASAP 2020 analyzer after degassing the samples at 150 °C for 5 h. X-ray photoelectron spectra (XPS) were recorded using a Kratos Axis-Ultra DLD instrument with a monochromatized $\text{Al K}\alpha$ line source ($h\nu = 1486.69$ eV), and with a concentric hemispherical analyzer working at 15 kV and 10 mA, and with the pressure of sample analysis chamber under high vacuum ($< 3 \times 10^{-9}$ Torr). The XPS analysis area was 300 × 700 μm , and the obtained spectra were referenced to C 1 s peak at 284.8 eV of adventitious carbon species. Fourier Transform Infrared spectra (FTIR) were investigated by a Bruker Vertex 70 FTIR spectrometer with a transmittance mode between 2000 and 500 cm^{-1} under a resolution of 4 cm^{-1} . Specimens for FTIR were obtained by mixing the dried samples and pre-dried KBr powder with a ratio of 0.4 wt% and then pressing into wafers. Raman spectra were obtained from 200 to 1200 cm^{-1} by a Lab RAM HR800 Raman spectrometer with an Ar^+ laser (20 mW, 514.532 nm) as excitation source.

2.3. Photoelectrochemical measurements

Photoelectrochemical measurements were carried out by a CH Instruments CHI 760D scanning potentiostat using a three-electrode cell, in which a Pt slice, Ag/AgCl and the as-prepared photoanodes were applied as the counter electrode, reference electrode and working anode, respectively. NaOH (1 M, pH = 13.6) aqueous solution was chosen as electrolyte. The photocurrent density (J-V) curves were recorded with a voltage scan rate of 0.01 V s⁻¹. Mott-Schottky (MS) curves were conducted with a constant frequency of 1 kHz under dark condition, and electrochemical impedance spectroscopy (EIS) were measured from 100 kHz to 1 Hz with a potential of 1.2 V vs Reversible Hydrogen Electrode (RHE) under irradiation. The following equation was used for the conversion between potential vs Ag/AgCl and potential vs RHE:

$$E_{\text{RHE}} = E_{\text{Ag/AgCl}} + 0.059 \times \text{pH} + E^\circ_{\text{Ag/AgCl}} \quad (\text{E}^\circ_{\text{Ag/AgCl}} \text{ is } 0.1976 \text{ V at } 25^\circ\text{C})$$

2.4. Photocatalytic measurements

Photocatalytic O_2 -evolution activities under visible-light irradiation were measured in a Pyrex glass cell (270 mL) with a side window for external-light incidence. A 300 W Xe lamp with different UV-cutoff filters ($\lambda \geq 420, 450, 500, 530$ and 590 nm) was applied as light source. La_2O_3 as pH buffer was used to keep pH values of reacted solutions at around 8–9 while AgNO_3 as sacrificial agent was employed to consume photo-generated electrons in O_2 -evolution reaction [18]. Sample (0.050 g), La_2O_3 (0.200 g) and AgNO_3 (0.679 g) were sequentially added into deionized water (200 mL) with stirring. After purged by nitrogen gas to eliminate air, the suspension was irradiated under constant stirring and at a constant temperature (around 35 °C)

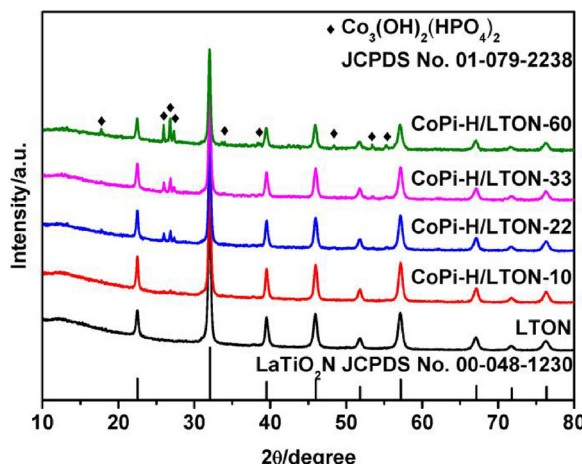


Fig. 1. XRD patterns for as-prepared LTON and CoPi-H/LTON- x ($x = 10, 22, 33, 60$).

controlled by thermostatic circulating water. The evolved O_2 was evaluated by a Beijing Beifen-Ruili Analytical Instrument SP-2100 gas chromatogram (TDX-01 column, thermal conductivity detector, Ar as carrier gas).

Apparent quantum yield (AQY) was evaluated under irradiation of the 300 W Xe lamp with a band-pass filter (425 nm). The irradiated light intensity was obtained by an Avantes AvaSpec-2048-USB2 spectrometer. The following equation was used to calculate the value of AQY:

$$\text{AQY} (\%) = \frac{\text{Number of reacted electrons}}{\text{Number of incident photons}} \times 100$$

$$= \frac{\text{Number of evolved } O_2 \text{ molecules} \times 4}{\text{Number of incident photons}} \times 100$$

3. Results and discussion

XRD patterns for as-prepared samples are shown in Fig. 1 and S1. LTON and CoPi-H showed diffraction peaks corresponding to LaTiO_2N (JCPDS No. 00-048-1230) and $\text{Co}_3(\text{OH})_2(\text{HPO}_4)_2$ (JCPDS No. 01-079-2238), respectively, proving the successful preparation of LaTiO_2N and $\text{Co}_3(\text{OH})_2(\text{HPO}_4)_2$. As for a series of CoPi-H/LTON- x ($x = 10, 22, 33, 60$), three peaks attributed to the characteristic peaks of $\text{Co}_3(\text{OH})_2(\text{HPO}_4)_2$ were observed in the range from 25 to 30° besides the characteristic peaks of LaTiO_2N , indicating that composites of LaTiO_2N and $\text{Co}_3(\text{OH})_2(\text{HPO}_4)_2$ were successfully prepared by the hydrothermal method and the introduction of $\text{Co}_3(\text{OH})_2(\text{HPO}_4)_2$ had no obvious influence on crystalline structure of LaTiO_2N . Moreover, intensities of the three characteristic peaks of $\text{Co}_3(\text{OH})_2(\text{HPO}_4)_2$ in the composites gradually increased with higher value of x , and other characteristic peaks of $\text{Co}_3(\text{OH})_2(\text{HPO}_4)_2$ for CoPi-H/LTON-60 were also observed, implying that the contents of $\text{Co}_3(\text{OH})_2(\text{HPO}_4)_2$ gradually increased in the composites.

Microstructures for as-prepared samples are observed from SEM and (HR)TEM images shown in Fig. 2, S2 and S3. Irregular brick-like chunks with porous surfaces for LTON were clearly observed in Fig. 2a and S3a [44]. Meanwhile, lattice fringes attributed to (112) and (022) lattice planes of LaTiO_2N were seen in Fig. S3b. As for the composites, it was clearly observed that nano-needles intricately grew on the porous surfaces of irregular brick-like chunks of LaTiO_2N (Fig. 2b and S2a,b,c), which indicated that these nano-needles were assigned to $\text{Co}_3(\text{OH})_2(\text{HPO}_4)_2$ combined with the XRD results and TEM images of CoPi-H/LTON-33 (Fig. 2c and S3c). As observed from the HRTEM image for CoPi-H/LTON-33 in Fig. 2d, lattice fringes belong to (−221) and (111) lattice planes of $\text{Co}_3(\text{OH})_2(\text{HPO}_4)_2$ were obviously seen on the nano-needles, further proving that the nano-needles were attributed

to $\text{Co}_3(\text{OH})_2(\text{HPO}_4)_2$. Meanwhile, lattice fringes belong to (004) lattice plane of LaTiO_2N were also clearly observed in adjacent areas of $\text{Co}_3(\text{OH})_2(\text{HPO}_4)_2$ nano-needles. It indicated that LaTiO_2N serving as substrates induced the growth of $\text{Co}_3(\text{OH})_2(\text{HPO}_4)_2$ nano-needles, thus forming close combination at the interface between LaTiO_2N and $\text{Co}_3(\text{OH})_2(\text{HPO}_4)_2$. Moreover, with the value of x increasing, nano-needles of $\text{Co}_3(\text{OH})_2(\text{HPO}_4)_2$ on the porous surfaces of LaTiO_2N became denser, and almost completely covered the porous surfaces for CoPi-H/LTON-60. It further implied that the content of $\text{Co}_3(\text{OH})_2(\text{HPO}_4)_2$ in the composites gradually increased with higher value of x , which was matched with XRD results. Additional nanoparticles appeared for CoPi-H/LTON-60 (Fig. S2c), which might be attributed to second growth of $\text{Co}_3(\text{OH})_2(\text{HPO}_4)_2$ after covering of $\text{Co}_3(\text{OH})_2(\text{HPO}_4)_2$ nano-needles on the porous surfaces of LaTiO_2N . In addition, pure CoPi-H consisted of irregularly aggregated micro-chunks (Fig. S2d) [42], which were completely different from $\text{Co}_3(\text{OH})_2(\text{HPO}_4)_2$ nano-needles in CoPi-H/LTON- x samples. It implied that the microstructures of $\text{Co}_3(\text{OH})_2(\text{HPO}_4)_2$ were extremely influenced by the introduced growing substrates of LaTiO_2N . Consequently, $\text{Co}_3(\text{OH})_2(\text{HPO}_4)_2/\text{LaTiO}_2\text{N}$ composites with a special microstructure were successfully constructed by in-situ hydrothermally growing $\text{Co}_3(\text{OH})_2(\text{HPO}_4)_2$ nano-needles on the surfaces of LaTiO_2N irregular brick-like chunks. Besides, BET surface areas of the composites (Table S1) firstly increased and then decreased with more $\text{Co}_3(\text{OH})_2(\text{HPO}_4)_2$. The decrease of surface areas for the composites was attributed to too high density of $\text{Co}_3(\text{OH})_2(\text{HPO}_4)_2$ nano-needles on the surfaces of LaTiO_2N according to SEM results.

As observed from UV-vis spectra (Fig. S4), LTON showed an absorption edge located at 600 nm corresponding to a narrow bandgap of 2.1 eV, and thus could utilize visible light effectively [45,46]. CoPi-H exhibited strong absorption peaks at 472, 490, 532 and 574 nm and a wide absorption peak at around 682 nm in visible-light region [42]. For CoPi-H/LTON- x ($x = 10, 22, 33, 60$), absorption edges were almost located at the same positions as that for LTON.

FTIR spectra for LTON, CoPi-H/LTON-33 and CoPi-H are shown in Fig. 3. For LTON, two broad peaks were located in the ranges from 940 to 770 cm^{-1} (Peak I) and from 720 to 500 cm^{-1} (Peak II), respectively. Peak I was attributed to the vibration of $\text{Ti}(\text{O},\text{N})_6$ octahedra bonds, while Peak II was due to the $\text{Ti}(\text{O},\text{N})\text{-Ti}$ stretching modes [47]. The two broad peaks were also observed in CoPi-H/LTON-33, which meant that the introduction of $\text{Co}_3(\text{OH})_2(\text{HPO}_4)_2$ led to no obvious structural change of LaTiO_2N as proved by XRD, SEM and TEM results. Besides, CoPi-H/LTON-33 displayed peaks at 1299, 1096, 997 and 584 cm^{-1} , which were assigned to the characteristic peaks of $\text{Co}_3(\text{OH})_2(\text{HPO}_4)_2$ based on the FTIR spectrum of CoPi-H. Moreover, the characteristic peaks of $\text{Co}_3(\text{OH})_2(\text{HPO}_4)_2$ for CoPi-H/LTON-33 shifted slightly compared with those of CoPi-H, which might be partially attributed to the microstructure change from micro-chunks to nano-needles of $\text{Co}_3(\text{OH})_2(\text{HPO}_4)_2$.

To investigate chemical composition and elemental valence state in the near-surface region of as-prepared samples, XPS measurement was carried out (Fig. 4, S6 and Table S2). Firstly, XPS spectra of Ti 2p for LTON and CoPi-H/LTON-33 are displayed in Fig. 4a. The peaks at 457.7 and 463.4 eV for LTON were assigned to $2p_{3/2}$ and $2p_{1/2}$ of Ti^{4+} cations, respectively [48], and the other two weak peaks at 456.9 and 462.1 eV were assigned to Ti^{3+} species [48,49]. For the composites, peaks of Ti 2p gradually shifted to higher binding energies with higher value of x (Table S2). Co 2p spectra for CoPi-H/LTON-33 and CoPi-H are observed from Fig. 4b. For CoPi-H, the peaks at 782.0 and 798.0 eV were attributed to $2p_{3/2}$ and $2p_{1/2}$ of Co^{2+} cations, respectively, and the other two wide peaks at 785.8 and 803.2 eV were assigned to shake-up satellite signals of Co^{2+} cations, hence indicating that only Co^{2+} species existed in CoPi-H [42]. For CoPi-H/LTON-33, the peaks of Co^{2+} cations at 781.4 and 797.1 eV moved slightly to lower binding energies compared with those for CoPi-H. XPS spectra of P 2p for CoPi-H/LTON-33 and CoPi-H are shown in Fig. 4c. Two peaks corresponding to $2p_{3/2}$

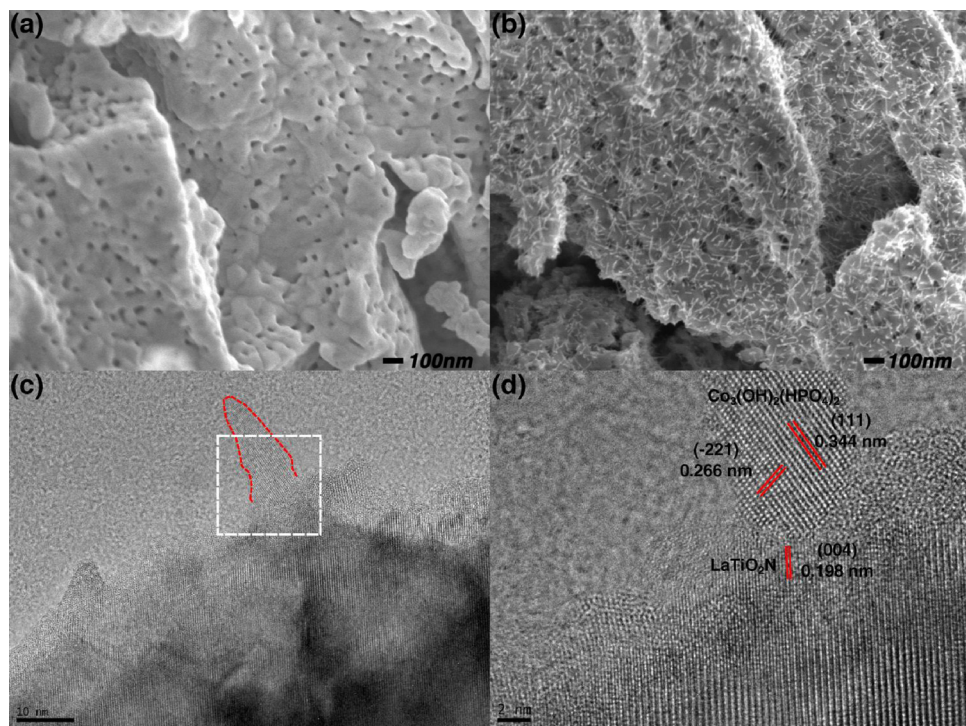


Fig. 2. (a) SEM image for LTON; (b) SEM and (c, d) HRTEM images for CoPi-H/LTON-33; (d) is the magnification area marked with white dashed line in (c). Scale bar: 100 nm (a, b); 10 nm (c); 2 nm (d).

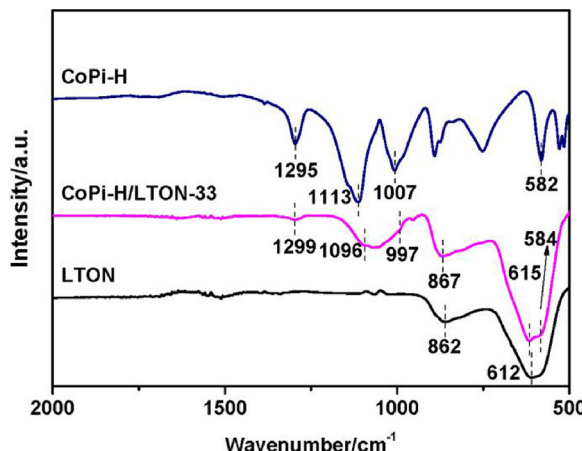


Fig. 3. FTIR spectra for LTON, CoPi-H/LTON-33 and CoPi-H.

and $2p_{1/2}$ of P^{5+} cations for CoPi-H were located at 133.5 and 134.4 eV [42], whereas the two peaks for CoPi-H/LTON-33 obviously shifted to lower binding energies. The shift of binding energies for Ti 2p, Co 2p and P 2p should be attributed to the interaction (electron transfer) between LaTiO_2N and $\text{Co}_3(\text{OH})_2(\text{HPO}_4)_2$ in the composites by close combination as proved by SEM and TEM results [50–53].

XPS spectra of O 1s for LTON, CoPi/LTON-33 and CoPi-H are exhibited in Fig. 4d. For LTON, the strong peak at 529.6 eV was due to O in the crystal lattice of LaTiO_2N [54], and the relatively weak peak at 531.2 eV was attributed to O in the surface hydroxyl groups ($-\text{OH}$) [55,56], and the peak at 533.0 eV was caused by O in chemisorbed water [56,57]. For CoPi-H/LTON-33, the peaks from O in crystal lattice, surface hydroxyl groups and absorbed water were located at 529.8, 531.7 and 533.3 eV, respectively, and shifted to higher energies compared with those for LTON. Moreover, as observed from Table S3, the contents of O in surface hydroxyl groups ($-\text{OH}$) gradually increased with higher value of x in the composites, which indicated that the

composites with more $\text{Co}_3(\text{OH})_2(\text{HPO}_4)_2$ had more hydroxyl groups on the surfaces. Furthermore, valence band (VB) spectra of LTON and CoPi-H are shown in Fig. S6a. The deduced valence band maximum (VBM) values for LTON and CoPi-H were around 1.29 and 1.89 eV (vs. the Fermi level (E_F)), respectively, thus indicating that the VBM of $\text{Co}_3(\text{OH})_2(\text{HPO}_4)_2$ was 0.6 eV more positive than that of LaTiO_2N .

Photocatalytic O_2 -evolution activities under visible-light irradiation ($\lambda \geq 420 \text{ nm}$) are exhibited in Fig. 5, S7 and Table S1. LTON showed considerable photocatalytic activity ($21.5 \mu\text{mol h}^{-1}$) in good consistent with references [44,58], while CoPi-H showed weak photocatalytic O_2 -evolution activity ($13.5 \mu\text{mol h}^{-1}$) as reported by our group recently [42]. As for CoPi-H/LTON- x ($x = 10, 22, 33, 60$), the photocatalytic activities were much higher than that for pure LaTiO_2N . Photocatalytic activities gradually increased at first and then decreased with higher value of x in the composites. Among them, CoPi-H/LTON-33 showed the highest photocatalytic activity ($74.3 \mu\text{mol h}^{-1}$), which was around 3.5 times that of LTON. Moreover, the estimated AQY of CoPi-H/LTON-33 reached up to 9.8% at 425 nm. Fig. 5b shows photocatalytic O_2 -evolution activities for CoPi-H/LTON-33 under visible-light irradiation with different cut-off filters ($\lambda \geq 420, 450, 500, 530$ and 590 nm). The obtained photocatalytic activities were in accordance with the light-absorption property, thus indicating that O_2 -evolution reaction on the composites was indeed promoted by the photons [17].

Besides, LTON-H had almost the same photocatalytic activity as LTON, implying that the hydrothermal treatment on LaTiO_2N had little effect on the photocatalytic O_2 -evolution activity. CoPi-H + LTON-33 showed higher photocatalytic activity than that of LTON, but lower than that of CoPi-H/LTON-33. Accordingly, on the one hand, the introduction of $\text{Co}_3(\text{OH})_2(\text{HPO}_4)_2$ on LaTiO_2N , by physical mixing or in-situ hydrothermal growth, could improve the photocatalytic activity. On the other hand, the strategy of in-situ hydrothermal growth was much more effective than that of physical mixing because of the close combination between LaTiO_2N and $\text{Co}_3(\text{OH})_2(\text{HPO}_4)_2$.

In order to explore the mechanism on the enhancement of photocatalytic water oxidation for the $\text{Co}_3(\text{OH})_2(\text{HPO}_4)_2/\text{LaTiO}_2\text{N}$ composites, photoelectrochemical properties of LTON and CoPi-H/LTON

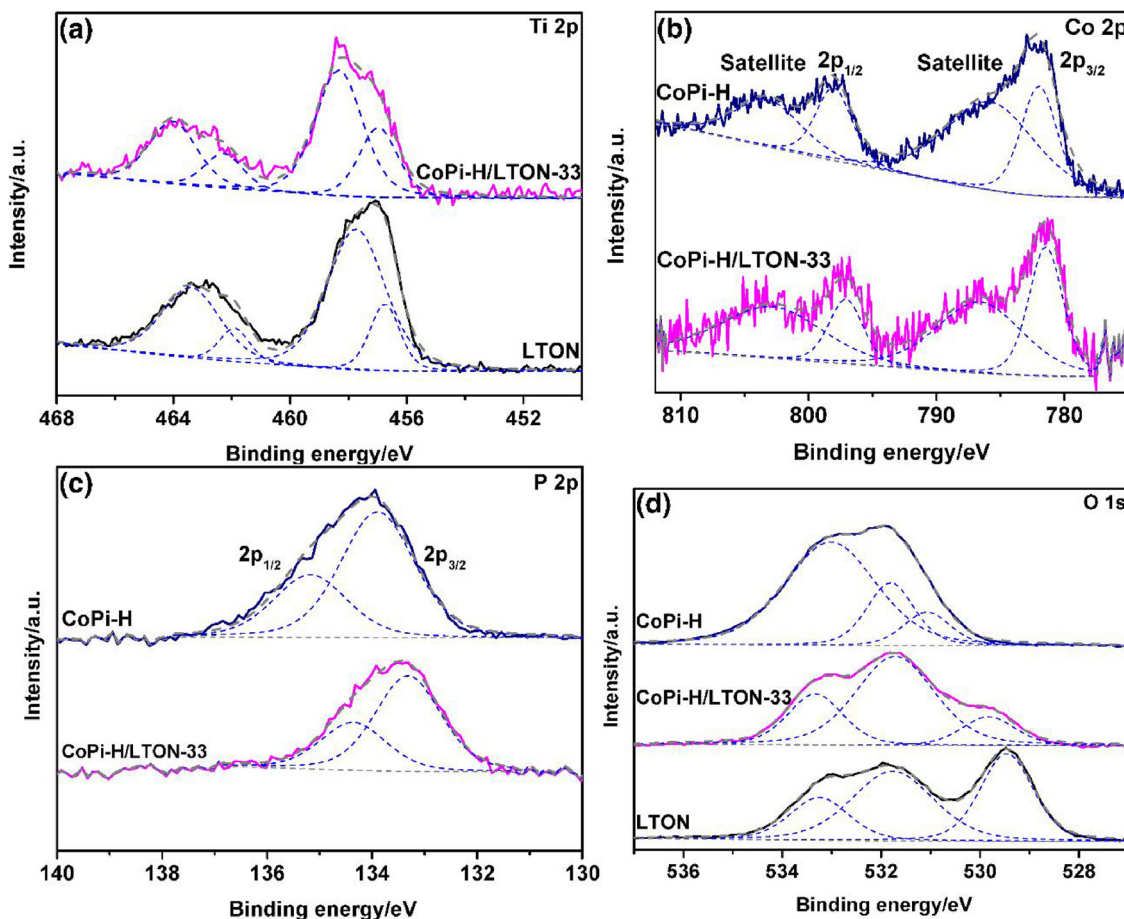


Fig. 4. (a) Ti 2p XPS spectra for LTON and CoPi-H/LTON-33, (b) Co 2p and (c) P 2p XPS spectra for CoPi-H/LTON-33 and CoPi-H, (d) O 1s XPS spectra for LTON, CoPi-H/LTON-33 and CoPi-H.

photoanodes were investigated. Photocurrent density-potential (J-V) curves (Fig. 6a) showed that CoPi-H/LTON photoanode had much higher photocurrent density than LTON photoanode. Moreover, EIS results (Fig. 6b and S11a) showed that CoPi-H/LTON photoanode, compared with LTON photoanode, had a much smaller arc radius, indicating the faster interfacial charge transport in $\text{Co}_3(\text{OH})_2(\text{HPO}_4)_2$ /LaTiO₂N composites than that in LaTiO₂N [61]. It further implied that the combination between $\text{Co}_3(\text{OH})_2(\text{HPO}_4)_2$ and LaTiO₂N would greatly enhance the separation and transfer of photo-generated charge carriers

in photocatalytic process for water oxidation [59,60]. Besides, Mott-Schottky plot for LTON photoanode (Fig. S11b) exhibited that LaTiO₂N had a flat-band potential of -0.52 V vs RHE. Considering the insulating n-type semiconducting character of LaTiO₂N, the calculated conduction band minimum (CBM) of LaTiO₂N was located at -0.62 eV vs RHE, which was in accordance with literature [61]. Therefore, the calculated VBM of LaTiO₂N was located at $+1.48$ eV vs RHE according to the band gap value of 2.1 eV. Based on the result of VB spectra that the VBM of $\text{Co}_3(\text{OH})_2(\text{HPO}_4)_2$ was 0.6 eV more positive than the VBM of LaTiO₂N,

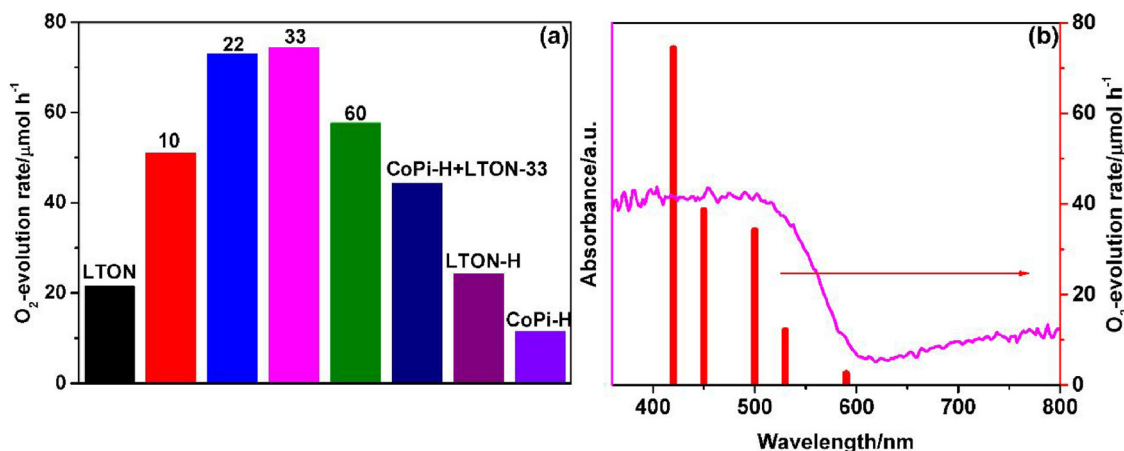


Fig. 5. (a) Photocatalytic O_2 -evolution rates (the first hour) under visible-light irradiation ($\lambda \geq 420$ nm) for as-prepared LTON, CoPi-H/LTON- x ($x = 10, 22, 33, 60$), CoPi-H, LTON-H and CoPi-H + LTON-33; (b) Photocatalytic O_2 -evolution rates (the first hour) for CoPi-H/LTON-33 under visible-light irradiation with different cut-off filters ($\lambda \geq 420, 450, 500, 530$ and 590 nm).

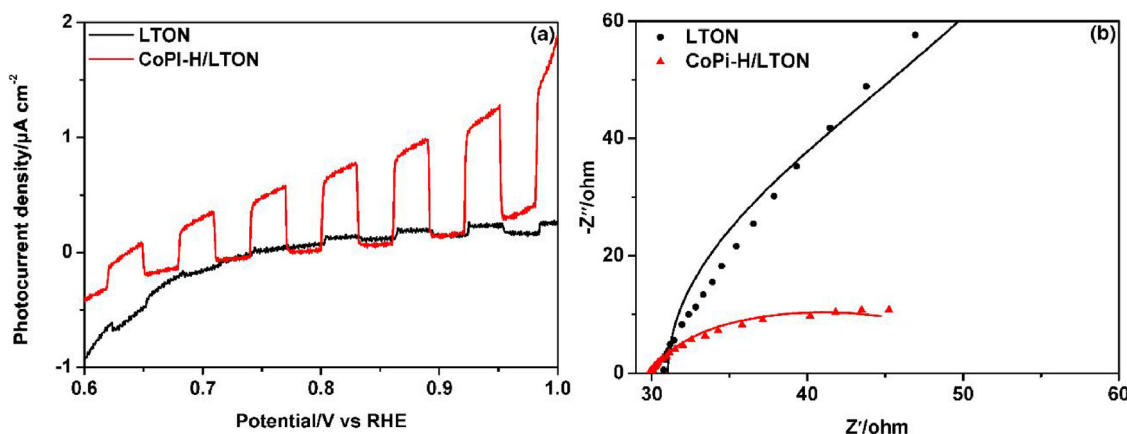


Fig. 6. (a) Photocurrent density-potential (J - V) curves and (b) Electrochemical impedance spectra (EIS) for LTON and CoPi-H/LTON photoanodes.

the calculated VBM of $\text{Co}_3(\text{OH})_2(\text{HPO}_4)_2$ was located at +2.08 eV vs RHE. According to our previous report and above UV-vis results (Fig. S4), the band-to-band absorption edge of $\text{Co}_3(\text{OH})_2(\text{HPO}_4)_2$ was located at around 313 nm and absorption peaks in the visible-light range were located at 472, 490, 532, 574 and 682 nm [42]. Then the calculated CBM and potential positions of energy levels for $\text{Co}_3(\text{OH})_2(\text{HPO}_4)_2$ were -1.88, -0.54, -0.45, -0.25, -0.08 and +0.26 eV vs RHE, respectively.

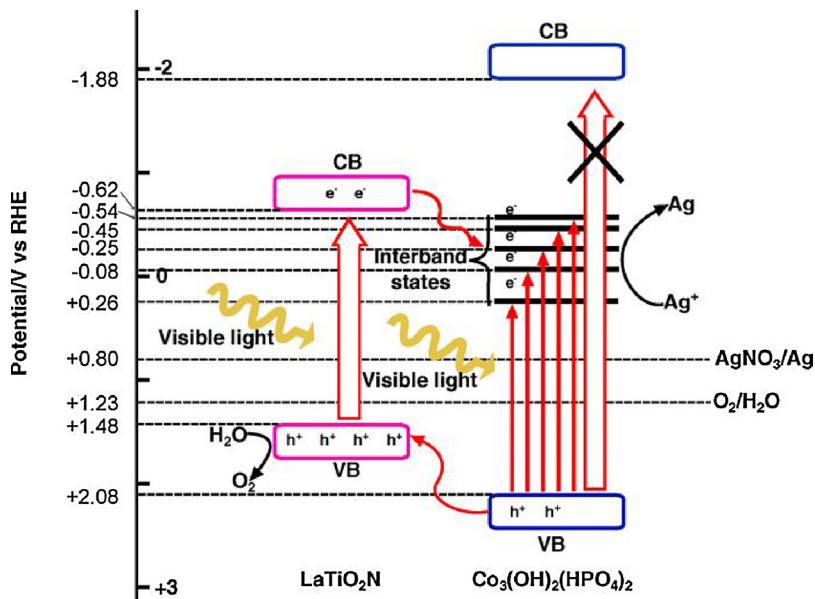
Based on the above analysis, the band structures and the separation and transfer routes of photo-generated carriers in $\text{Co}_3(\text{OH})_2(\text{HPO}_4)_2/\text{LaTiO}_2\text{N}$ composite photocatalyst with a heterojunction structure were schematically illustrated in Scheme 1. Firstly, both LaTiO_2N and $\text{Co}_3(\text{OH})_2(\text{HPO}_4)_2$ produce photo-generated carriers under visible-light irradiation. Then photo-generated holes shift from the valence band (VB) of $\text{Co}_3(\text{OH})_2(\text{HPO}_4)_2$ to the VB of LaTiO_2N at more negative position, while photo-generated electrons transfer from the conduction band (CB) of LaTiO_2N to interband states of $\text{Co}_3(\text{OH})_2(\text{HPO}_4)_2$ at more positive positions. Finally, water oxidation reaction happens on the surfaces of LaTiO_2N , and photo-generated electrons in the interband states of $\text{Co}_3(\text{OH})_2(\text{HPO}_4)_2$ react with Ag^+ to produce Ag .

According to the above analysis, in such a heterojunction of $\text{Co}_3(\text{OH})_2(\text{HPO}_4)_2/\text{LaTiO}_2\text{N}$, the matched band structures in the composites accelerated the separation and transfer of photo-generated carriers. Meanwhile, compared with the micro-chunk structure of

$\text{Co}_3(\text{OH})_2(\text{HPO}_4)_2$ in pure CoPi-H, the nano-needle structure of $\text{Co}_3(\text{OH})_2(\text{HPO}_4)_2$ in CoPi-H/LTON-33 could effectively shorten the transfer distance of photo-generated carriers to the surface and thus shorten the corresponding transfer time [62]. It was therefore implied that the nano-needle structure of $\text{Co}_3(\text{OH})_2(\text{HPO}_4)_2$, besides the heterojunction structure of $\text{Co}_3(\text{OH})_2(\text{HPO}_4)_2/\text{LaTiO}_2\text{N}$, should be favorable for the separation and transfer of photo-generated carriers as well.

Moreover, the close interfacial combination between in-situ grown $\text{Co}_3(\text{OH})_2(\text{HPO}_4)_2$ nano-needles and LaTiO_2N substrates enhanced the function of $\text{Co}_3(\text{OH})_2(\text{HPO}_4)_2/\text{LaTiO}_2\text{N}$ heterojunction. In addition, the highly proportional surface hydroxide groups, which existed in the $\text{Co}_3(\text{OH})_2(\text{HPO}_4)_2/\text{LaTiO}_2\text{N}$ composites, could accelerate proton transfer at the surfaces of photocatalysts according to previous reports [63–66]. Consequently, the favorable electronic configurations and interface/surface characteristics synergistically promoted photocatalytic water oxidation on the hydrothermally prepared composites.

As for CoPi-H/LTON-60, the decreased photocatalytic activity compared with that of CoPi-H/LTON-33 might be caused by the following factors. The O_2 -evolution reaction mainly happened on the surfaces of LaTiO_2N in the $\text{Co}_3(\text{OH})_2(\text{HPO}_4)_2/\text{LaTiO}_2\text{N}$ composites. $\text{Co}_3(\text{OH})_2(\text{HPO}_4)_2$ nano-needles with too high density on the surfaces of LaTiO_2N decreased reactive sites for O_2 evolution, and prevented water molecules in aqueous solution from reacting with photo-generated holes on the surfaces of LaTiO_2N , and hindered the intimate contact



Scheme 1. Schematic illustration of the band structures and the separation and transfer routes of photo-generated carriers in $\text{Co}_3(\text{OH})_2(\text{HPO}_4)_2/\text{LaTiO}_2\text{N}$ composite photocatalyst.

between $\text{Co}_3(\text{OH})_2(\text{HPO}_4)_2$ and LaTiO_2N to form heterojunctions. Besides, the rates of photocatalytic O_2 evolution for the $\text{Co}_3(\text{OH})_2(\text{HPO}_4)_2/\text{LaTiO}_2\text{N}$ composites gradually decreased with longer reaction time (Fig. S7). This phenomenon is commonly observed in photocatalytic water oxidation with AgNO_3 as sacrificial agents [67], and explained as follows. During the photocatalytic process, metallic Ag was reduced from Ag^+ , and gradually covered the surfaces of photocatalysts, hindering light absorption and diminishing reactive sites [13,42,68].

4. Conclusions

$\text{Co}_3(\text{OH})_2(\text{HPO}_4)_2$ nano-needles were successfully in-situ grown on the porous surfaces of LaTiO_2N irregular brick-like chunks to form a series of composite photocatalysts with different ratios of $\text{Co}_3(\text{OH})_2(\text{HPO}_4)_2$ and LaTiO_2N by a hydrothermal process. The matched band structures and the close interfacial combination between $\text{Co}_3(\text{OH})_2(\text{HPO}_4)_2$ and LaTiO_2N in the composites ensured the formation of effective heterojunction, which facilitated the separation and transfer of photo-generated carriers. As a result, photocatalytic activity on the $\text{Co}_3(\text{OH})_2(\text{HPO}_4)_2/\text{LaTiO}_2\text{N}$ composites was enhanced up to 3.5 times that on LaTiO_2N . This work provides a feasible approach to couple cobalt phosphate with special micro/nano-structures on host photocatalysts for improved photocatalytic performance.

Competing financial interests

The authors declare no competing financial interest.

Acknowledgments

This work is supported by the National Natural Science Foundation of China (Nos. 51302212 and 51502240), the China Postdoctoral Science Foundation (Nos. 2014T70915 and 2013M540745), the Postdoctoral Science Foundation in Shaanxi Province of China, the Natural Science Basic Research Plan in Shaanxi Province of China (No. 2014JQ2-5022), and the Fundamental Research Funds for the Central Universities. We also thank Penghui Guo (Engineer, International Research Center for Renewable Energy (IRCRE), State Key Laboratory of Multiphase Flow in Power Engineering (MFPE), Xi'an Jiaotong University, Xi'an 710049, China) for helpful discussion and revisions of this manuscript, and appreciate the help of Chuansheng Ma (Engineer, Jia-Lab for Interface and Atomic Structure, Xi'an Jiaotong University, Xi'an 710049, China) for assistance to obtain better TEM images.

Appendix A. Supplementary data

Supplementary material related to this article can be found, in the online version, at doi:<https://doi.org/10.1016/j.apcatb.2018.03.067>.

References

- [1] T. Hisatomi, J. Kubota, K. Domen, Chem. Soc. Rev. 43 (2014) 7520–7535.
- [2] W. Wang, M.O. Tadé, Z. Shao, Chem. Soc. Rev. 44 (2015) 5371–5408.
- [3] T.A. Betley, Q. Wu, T. Van Voorhis, D.G. Nocera, Inorg. Chem. 47 (2008) 1849–1861.
- [4] S.J. Moniz, S.A. Shevlin, D.J. Martin, Z.-X. Guo, J. Tang, Energy Environ. Sci. 8 (2015) 731–759.
- [5] A. Kudo, Y. Miseki, Chem. Soc. Rev. 38 (2009) 253–278.
- [6] G. Hitoki, T. Takata, J.N. Kondo, M. Hara, H. Kobayashi, K. Domen, Chem. Commun. (2002) 1698–1699.
- [7] K. Maeda, R. Abe, K. Domen, J. Phys. Chem. C 115 (2011) 3057–3064.
- [8] M. Hojamberdiev, K. Yubuta, J.J.M. Vequizo, A. Yamakata, S. Oishi, K. Domen, K. Teshima, Cryst. Growth Des. 15 (2015) 4663–4671.
- [9] K. Maeda, K. Domen, Angew. Chem. Int. Ed. 51 (2012) 9865–9869.
- [10] K. Maeda, D. Lu, K. Domen, Angew. Chem. Int. Ed. 52 (2013) 6488–6491.
- [11] K. Kawashima, M. Hojamberdiev, H. Wagata, K. Yubuta, J.J.M. Vequizo, A. Yamakata, S. Oishi, K. Domen, K. Teshima, J. Phys. Chem. C 119 (2015) 15896–15904.
- [12] Y. Li, F. Li, X. Li, H. Song, Z. Lou, Z. Ye, L. Zhu, Nano Energy 19 (2016) 437–445.
- [13] F. Zhang, A. Yamakata, K. Maeda, Y. Moriya, T. Takata, J. Kubota, K. Teshima, S. Oishi, K. Domen, J. Am. Chem. Soc. 134 (2012) 8348–8351.
- [14] Y. Zhou, G. Chen, Y. Yu, L. Zhao, Q. Yu, Q. He, Catal. Sci. Technol. 6 (2016) 1033–1041.
- [15] H.J. Kong, D.H. Won, J. Kim, S.I. Woo, Chem. Mater. 28 (2016) 1318–1324.
- [16] S. Nayak, L. Mohapatra, K. Parida, J. Mater. Chem. A 3 (2015) 18622–18635.
- [17] G. Zhang, S. Zang, X. Wang, ACS Catal. 5 (2015) 941–947.
- [18] A. Kasahara, K. Nukumizu, T. Takata, J.N. Kondo, M. Hara, H. Kobayashi, K. Domen, J. Phys. Chem. B 107 (2003) 791–797.
- [19] X. Wang, Z. Li, Z. Zou, Phys. Chem. Chem. Phys. 17 (2015) 19631–19636.
- [20] Y. Li, X. Cheng, X. Ruan, H. Song, Z. Lou, Z. Ye, L. Zhu, Nano Energy 12 (2015) 775–784.
- [21] M. Matsukawa, R. Ishikawa, T. Hisatomi, Y. Moriya, N. Shibata, J. Kubota, Y. Ikuhara, K. Domen, Nano Lett. 14 (2014) 1038–1041.
- [22] K. Kawashima, M. Hojamberdiev, H. Wagata, M. Nakayama, K. Yubuta, S. Oishi, K. Domen, K. Teshima, Catal. Sci. Technol. 6 (2016) 5389–5396.
- [23] W. Luo, Z. Li, X. Jiang, T. Yu, L. Liu, X. Chen, J. Ye, Z. Zou, Phys. Chem. Chem. Phys. 10 (2008) 6717–6723.
- [24] A.E. Maegli, T. Hisatomi, E.H. Otal, S. Yoon, S. Pokrant, M. Grätzel, A. Weidenkaff, J. Mater. Chem. 22 (2012) 17906–17913.
- [25] N. Umezawa, A. Janotti, ChemSusChem 9 (2016) 1027–1031.
- [26] C.M. Leroy, A.E. Maegli, K. Sivula, T. Hisatomi, N. Xanthopoulos, E.H. Otal, S. Yoon, A. Weidenkaff, R. Sanjines, M. Grätzel, Chem. Commun. 48 (2012) 820–822.
- [27] Q. Yin, J.M. Tan, C. Besson, Y.V. Geletii, D.G. Musaev, A.E. Kuznetsov, Z. Luo, K.I. Hardcastle, C.L. Hill, Science 328 (2010) 342–345.
- [28] D.P. Kumar, H. Park, E.H. Kim, S. Hong, M. Gopannagari, D.A. Reddy, T.K. Kim, Appl. Catal. B: Environ. 224 (2018) 230–238.
- [29] G. Gardner, J. Al-Sharab, N. Danilovic, Y.B. Go, K. Ayers, M. Greenblatt, G.C. Dismukes, Energy Environ. Sci. 9 (2016) 184–192.
- [30] F. Jiao, H. Frei, Energy Environ. Sci. 3 (2010) 1018–1027.
- [31] K. Maeda, K. Ishimaki, M. Okazaki, T. Kanazawa, D. Lu, S. Nozawa, H. Kato, M. Kakihana, ACS Appl. Mater. Interfaces 9 (2017) 6114–6122.
- [32] F. Song, X. Hu, J. Am. Chem. Soc. 136 (2014) 16481–16484.
- [33] Y. Li, L. Zhang, X. Xiang, D. Yan, F. Li, J. Mater. Chem. A 2 (2014) 13250–13258.
- [34] Y. Dou, S. Zhang, T. Pan, S. Xu, A. Zhou, M. Pu, H. Yan, J. Han, M. Wei, D.G. Evans, Adv. Funct. Mater. 25 (2015) 2243–2249.
- [35] S.J. Kim, Y. Lee, D.K. Lee, J.W. Lee, J.K. Kang, J. Mater. Chem. A 2 (2014) 4136–4139.
- [36] Y. Liu, H. Cheng, M. Lyu, S. Fan, Q. Liu, W. Zhang, Y. Zhi, C. Wang, C. Xiao, S. Wei, J. Am. Chem. Soc. 136 (2014) 15670–15675.
- [37] M.-R. Gao, Y.-F. Xu, J. Jiang, Y.-R. Zheng, S.-H. Yu, J. Am. Chem. Soc. 134 (2012) 2930–2933.
- [38] G. Zhang, S. Zang, Z.-A. Lan, C. Huang, G. Li, X. Wang, J. Mater. Chem. A 3 (2015) 17946–17950.
- [39] M. Barroso, A.J. Cowan, S.R. Pendlebury, M. Grätzel, D.R. Klug, J.R. Durrant, J. Am. Chem. Soc. 133 (2011) 14868–14871.
- [40] M.W. Kanan, Y. Surendranath, D.G. Nocera, Chem. Soc. Rev. 38 (2009) 109–114.
- [41] D. Wang, R. Li, J. Zhu, J. Shi, J. Han, X. Zong, C. Li, J. Phys. Chem. C 116 (2012) 5082–5089.
- [42] Y. Zhang, J. Shi, Y. Hu, Z. Huang, L. Guo, Catal. Sci. Technol. 6 (2016) 8080–8088.
- [43] J. Feng, W. Luo, T. Fang, H. Lv, Z. Wang, J. Gao, W. Liu, T. Yu, Z. Li, Z. Zou, Adv. Funct. Mater. 24 (2014) 3535–3542.
- [44] A.E. Maegli, S. Pokrant, T. Hisatomi, M. Trottmann, K. Domen, A. Weidenkaff, J. Phys. Chem. C 118 (2013) 16344–16351.
- [45] A. Kasahara, K. Nukumizu, G. Hitoki, T. Takata, J.N. Kondo, M. Hara, H. Kobayashi, K. Domen, J. Phys. Chem. A 106 (2002) 6750–6753.
- [46] T. Minegishi, N. Nishimura, J. Kubota, K. Domen, Chem. Sci. 4 (2013) 1120–1124.
- [47] D. Li, W. Li, C. Fasel, J. Shen, R. Riedel, J. Alloys Compd. 586 (2014) 567–573.
- [48] N.G. Sarda, M. Omune, T. Hayashi, A. Chan, S. Kataoka, K.-I. Murai, G.I. Waterhouse, T. Moriga, J. Eur. Ceram. Soc. 35 (2015) 3311–3317.
- [49] M.C. Biesinger, L.W. Lau, A.R. Gerson, R.S.C. Smart, Appl. Surf. Sci. 257 (2010) 887–898.
- [50] S.-Z. Kang, L. Chen, X. Li, J. Mu, Appl. Surf. Sci. 258 (2012) 6029–6033.
- [51] D. Lin, H. Wu, R. Zhang, W. Pan, Chem. Mater. 21 (2009) 3479–3484.
- [52] Y. Liu, L. Yu, Y. Hu, C. Guo, F. Zhang, X.W.D. Lou, Nanoscale 4 (2012) 183–187.
- [53] Z. Zhang, C. Shao, X. Li, C. Wang, M. Zhang, Y. Liu, ACS Appl. Mater. Interfaces 2 (2010) 2915–2923.
- [54] Q.N. Pham, C. Bohnke, O. Bohnke, Surf. Sci. 572 (2004) 375–384.
- [55] N.A. Merino, B.P. Barbero, P. Eloy, L.E. Cadús, Appl. Surf. Sci. 253 (2006) 1489–1493.
- [56] A. Braun, F. Aksyo Akgul, Q. Chen, S. Erat, T.-W. Huang, N. Jabeen, Z. Liu, B.S. Mun, S.S. Mao, X. Zhang, Chem. Mater. 24 (2012) 3473–3480.
- [57] C.-Z. Yuan, Y.-F. Jiang, Z. Wang, X. Xie, Z.-K. Yang, A.B. Yousaf, A.-W. Xu, J. Mater. Chem. A 4 (2016) 8155–8160.
- [58] A.E. Maegli, E.H. Otal, T. Hisatomi, S. Yoon, C.M. Leroy, N. Schäuble, Y. Lu, M. Grätzel, A. Weidenkaff, Energy Procedia 22 (2012) 61–66.
- [59] S.S. Gujral, A.N. Simonov, M. Higashi, R. Abe, L. Spiccia, ChemElectroChem 2 (2015) 1270–1278.
- [60] Y. Li, R. Jin, Y. Xing, J. Li, S. Song, X. Liu, M. Li, R. Jin, Adv. Energy Mater. (2016) 6.
- [61] C. Le Paven-Thivet, A. Ishikawa, A. Ziani, L. Le Gendre, M. Yoshida, J. Kubota, F. Tessier, K. Domen, J. Phys. Chem. C 113 (2009) 6156–6162.
- [62] X. Chen, S. Shen, L. Guo, S.S. Mao, Chem. Rev. 110 (2010) 6503–6570.
- [63] H. Hussain, G. Tocci, T. Woolcot, X. Torrelles, C. Pang, D. Humphrey, C. Yim, D. Grinter, G. Cabailh, O. Bikondo, Nat. Mater. 16 (2017) 461–466.
- [64] C.-C. Chen, S.-H. Hu, Y.-P. Fu, J. Alloys Compd. 632 (2015) 326–334.
- [65] D. Zhang, M. Yang, S. Dong, J. Phys. Chem. C 119 (2015) 1451–1456.
- [66] S.-Y. Guo, S. Han, B. Chi, J. Pu, J. Li, Int. J. Hydrogen Energy 39 (2014) 2446–2453.
- [67] D.J. Martin, N. Umezawa, X. Chen, J. Ye, J. Tang, Energy Environ. Sci. 6 (2013) 3380–3386.
- [68] X. Guan, L. Guo, ACS Catal. 4 (2014) 3020–3026.